

Control of the asymmetric band structure in Mn₂Au by a ferromagnetic driver layer

Y. Lytvynenko,^{1,2} O. Fedchenko,¹ S. V. Chernov,¹ S. Babenkov,¹ D. Vasilyev,¹ O. Tkach,¹ A. Gloskovskii,³ T. R. F. Peixoto,³ C. Schlueter,³ V. Grigorev,^{1,4,5} M. Filianina,^{1,4,5} S. Sobolev,¹ A. Kleibert,⁶ M. Kläui,¹ J. Demsar,¹ G. Schönhense,¹ M. Jourdan,¹ and H. J. Elmers^{1,*}

¹*Institut für Physik, Johannes Gutenberg-Universität, Staudingerweg 7, D-55099 Mainz, Germany*


²*Institute of Magnetism of the NAS and MES of Ukraine, 03142 Kyiv, Ukraine*

³*Deutsches Elektronen-Synchrotron DESY, 22607 Hamburg, Germany*

⁴*Graduate School of Excellence Materials Science in Mainz, 55128 Mainz, Germany*

⁵*Department of Physics, AlbaNova University Center, Stockholm University, 10691 Stockholm, Sweden*

⁶*Paul Scherrer Institute, Swiss Light Source, 5232 Villigen, Switzerland*

 (Received 5 June 2023; revised 30 August 2023; accepted 5 September 2023; published 15 September 2023)

Hard x-ray angle-resolved photoemission spectroscopy reveals the momentum-resolved band structure in an epitaxial Mn₂Au(001) film capped by a 2-nm-thick ferromagnetic permalloy layer. By magnetizing the permalloy capping layer, the exceptionally strong exchange bias aligns the Néel vector in the Mn₂Au(001) film accordingly. Uncompensated interface Mn magnetic moments in Mn₂Au were identified as the origin of the exchange bias using x-ray magnetic circular dichroism in combination with photoelectron emission microscopy. Using time-of-flight momentum microscopy, we measure the asymmetry of the band structure, $E(k) \neq E(-k)$, in Mn₂Au resulting from the homogeneous orientation of the Néel vector. Comparison with theory shows that the Néel vector, determined by the magnetic moment of the top Mn layer, is antiparallel to the permalloy magnetization. The experimental results demonstrate that hard x-ray photoemission spectroscopy can measure the band structure of epitaxial layers beneath a metallic capping layer and corroborate the asymmetric band structure in Mn₂Au that was previously inferred only indirectly.

DOI: [10.1103/PhysRevB.108.104413](https://doi.org/10.1103/PhysRevB.108.104413)

I. INTRODUCTION

Antiferromagnets have attracted scientific interest as active materials in spintronics [1–3]. The orientation of the sublattice magnetization, defined as the Néel vector $\vec{N} = \vec{M}_1 - \vec{M}_2$, acts as an information carrier, where the anisotropic magnetoresistance effect allows to read out the Néel vector alignment [4]. Magnetic linear dichroism allows for an ultrafast optical read-out [5]. Electrical currents enable the manipulation of \vec{N} to write information, as has been demonstrated for CuMnAs [6–9] and Mn₂Au [4,10,11]. A second-order magnetoresistance has been observed in CuMnAs [12]. For Mn₂Au films spin to charge current conversion by the inverse spin Hall effect has been shown [13] as well as the electric field control of the Néel spin-orbit torque [14]. The current-induced manipulation of \vec{N} has been attributed to the Néel spin-orbit torque [2].

At the microscopic electronic-structure level, the control over the Néel vector allows manipulation of some electronic properties [15]. The manipulation of electronic states in Mn₂Au shows up as an asymmetry in the electronic band structure, $E(k) \neq E(-k)$ [16]. The usual band structure parity $E(k) = E(-k)$ results from the symmetries of the materials, such as inversion/parity \mathcal{P} , time-reversal coupled with translation $\mathcal{T}t$, or time-reversal coupled with the spin rotational

symmetry \mathcal{TR}_S (\mathcal{R}_S rotates the spin by 180°). In Mn₂Au these symmetries are broken. The asymmetric band structure is then caused by a Rashba-like mechanism in combination with the staggered magnetization in Mn₂Au [17,18].

Predictions for the occurrence of antiferromagnetic parity violation have been given for spin-orbit coupled collinear antiferromagnets such as CuMnAs and Mn₂Au, which break \mathcal{P} and \mathcal{T} symmetries but preserve the combined \mathcal{PT} symmetry [17,19–22]. Despite having crystal parity, the antiferromagnetic order breaks this symmetry in the presence of spin-orbit coupling. The direct observation of parity violation in Mn₂Au using angle- and space-resolved photoemission spectroscopy (ARPES) was reported in Ref. [16].

The occurrence of band asymmetry is not restricted to these two systems but also shows up at interfaces of collinear antiferromagnets, as reported for GdIr₂Si₂ [23], and for Ag₂Bi-terminated Ag films [24]. Asymmetric band structures have also been predicted to occur in complex noncoplanar magnets that break the \mathcal{TR}_S symmetry [19]. However, in these systems, the Néel vector is determined by the crystal structure and cannot be manipulated by current.

The presence of small antiferromagnetic domains in Mn₂Au [25,26] is generally an obstacle to angle-resolved photoemission spectroscopy, which then requires both angular and spatial resolution [16]. As we have shown previously [26], it is possible to align the Néel vector using a ferromagnetic permalloy driver layer deposited on top of the Mn₂Au film by exploiting the strong exchange bias between Mn₂Au and

*elmerts@uni-mainz.de

permalloy. The remaining questions are what is the relative orientation of the Néel vector and the magnetization in the permalloy driver layer, and can one observe the controlling of the band structure in Mn_2Au beneath the driver layer.

In this paper, we confirm the control of the asymmetric band structure in a $\text{Mn}_2\text{Au}(001)$ film by the remanent magnetization in the permalloy layer. We show that $\vec{N} \cdot \vec{M}$ is negative, i.e., the Néel vector \vec{N} is antiparallel to the permalloy magnetization \vec{M} .

We use hard x-ray angular resolved photoemission spectroscopy to determine the electronic structure of $\text{Mn}_2\text{Au}(001)$ films below the capping layer utilizing the increased inelastic mean free path of high-energy photoexcited electrons. Here, the permalloy layer is polycrystalline and therefore only adds an angular-independent photoemission intensity to the background. The asymmetry in the band structure observed in the photoemission experiment defines the direction of the Néel vector.

II. EXPERIMENTAL DETAILS

All layers of the $\text{Mn}_2\text{Au}(001)(45 \text{ nm})/\text{Ni}_{80}\text{Fe}_{20}(\text{Py})(2 \text{ nm})/\text{SiN}_x(1.8 \text{ nm})$ samples were deposited by RF sputtering on epitaxial $\text{Ta}(001)(13 \text{ nm})$ single or $\text{Ta}(001)(13 \text{ nm})/\text{Mo}(001)(20 \text{ nm})$ double buffer layers on the $\text{Al}_2\text{O}_3(\text{r-plane})$ or $\text{MgO}(100)$ substrates, respectively. The details of the deposition process are described in Refs. [21,27,28]. The permalloy and SiN_x layers were deposited at room temperature and form polycrystalline films. Note that the sketched pseudomorphic growth of permalloy on $\text{Mn}_2\text{Au}(001)$ in Fig. 1(f) just indicates the atomic layers. In fact, permalloy has a face centered cubic structure and grows in a fine-grained polycrystalline or even amorphous structure on the Mn_2Au surface as confirmed by x-ray diffraction [26]. SiN_x is an oxidation-preventing capping layer, and is highly transparent to photoemitted electrons [21]. Rectangular magnetic hysteresis loops of the samples, measured using a Quantum Design MPMS SQUID-magnetometer, confirm that the saturation magnetization in permalloy is equal to the remanent magnetization (square-shaped hysteresis loop). Magnetic alignment of $\text{Mn}_2\text{Au}(001)/\text{Py}$ samples was performed in a magnetic field up to 1 T applied in four different easy crystallographic directions $\langle 110 \rangle$ of Mn_2Au . For some samples, the permalloy layer was not added to allow for reference measurements in the as grown multidomain state of the antiferromagnetic Mn_2Au film.

Hard x-ray photoemission spectroscopy was performed at beamline P22 of the storage ring PETRA III at DESY in Hamburg using time-of-flight momentum microscopy [29] at a sample temperature of 20 K. Due to the high energy (6.0 GeV) and the large size (2.3 km circumference) of PETRA, P22 provides hard x-ray radiation with high brilliance in an energy range from 2.4 to 15 keV. The experimental conditions were 2×10^{13} photons/s at 5.210 keV in a spot of about $50 \times 50 \mu\text{m}^2$ using a $\text{Si}(311)$ double-crystal monochromator [30]. The total energy resolution is governed by the photon band width of 155 meV.

The inelastic mean free path of photoexcited electrons with a kinetic energy of 5 keV is $\lambda_{\text{MFP}} = 4 \text{ nm}$ independent of the material according to Ref. [31]. The penetration depth of the

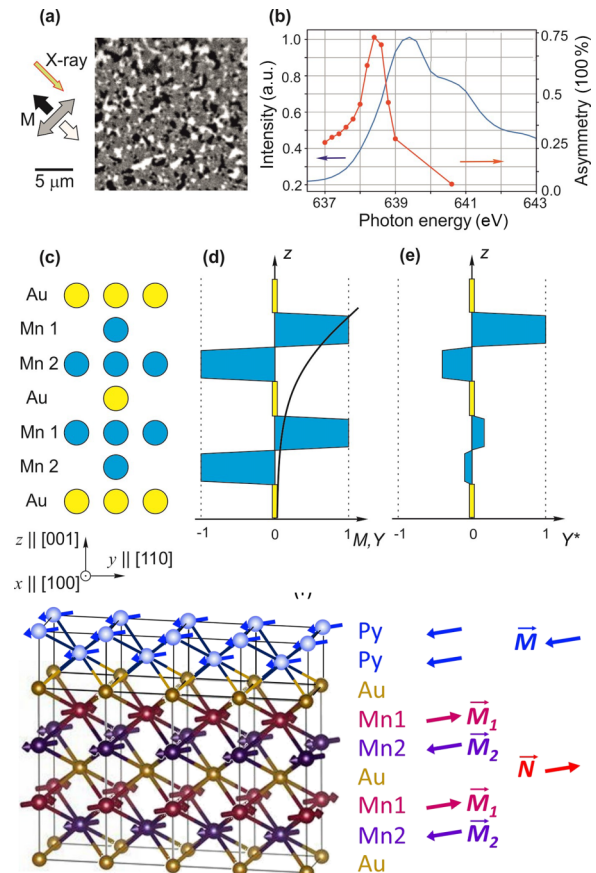


FIG. 1. (a) XMCD-PEEM image ($20 \times 20 \mu\text{m}^2$) of the $\text{Mn}_2\text{Au}(100)$ film capped with a thin SiN layer measured at the photon energy of 638.5 eV. Black and white contrast levels indicate the XMCD asymmetry of opposite sign, whereas the intermediate contrast level indicates a vanishing XMCD asymmetry, corresponding to the domains with Néel vector aligned perpendicular to the x-ray propagation direction (see schematic to the left of the XMCD asymmetry image). (b) X-ray absorption spectrum (blue full line) and XMCD asymmetry (red dots) vs photon energy. (c) Two-dimensional sketch of the layered crystal structure of Mn_2Au . (d) Sketch of the electron yield Y for an atomic layer and the atomic layer magnetization M vs depth z . (e) Resulting contribution Y^* of the atomic layers to the total XMCD asymmetry, showing that the prevailing component stems from the top Mn layer. (f) Three-dimensional sketch of the $\text{Mn}_2\text{Au}/\text{permalloy}$ structure indicating the Néel vector \vec{N} and permalloy magnetization \vec{M} .

x-ray radiation is much larger. In this case, the inelastic mean free path limits the resolution of the perpendicular momentum to $\Delta k_z = 1/\lambda_{\text{MFP}} = 0.024 \text{ \AA}^{-1}$. The (normalized) contribution to the signal from a layer at a depth z is given by $I_0 dz = \exp(-z/\lambda_{\text{MFP}})$, where I_0 is the density of photoexcited electrons that is proportional to the incident x-ray intensity. In our case of a 2-nm-thick capping layer, integrating its contribution from the depth $z = 0$ to $z = 2 \text{ nm}$ gives $I_{\text{PY}} = I_0 1.6 \text{ nm}$. A similar integration results in a contribution of $I_{\text{AF}} = I_0 2.4 \text{ nm}$ from the Mn_2Au film. This means that we expect 40% of the photoemission intensity to come from the permalloy layer and 60% from the antiferromagnetic layer.

To distinguish asymmetries due to the Néel vector reorientation from asymmetries caused by the detector response

function or by a dichroism from the photoemission process itself, we carried out the experiment such that the magnetization in the permalloy capping layer is the only varied parameter. For hard x-ray measurements with defined orientation of the Néel vector direction, we cut each $1 \times 1 \text{ cm}^2$ film into four pieces, $5 \times 5 \text{ mm}^2$ each. We then mounted the four pieces on the same sample holder, where for each piece the permalloy layer was magnetized prior to mounting in one of the four easy magnetic directions of Mn_2Au along the $\langle 110 \rangle$ crystal axes. Photoemission data were then recorded separately for each of the four mounted pieces. Previous x-ray diffraction and photoemission experiments confirmed homogeneous sample properties over the cm^2 -sized sample. We can thus safely assume that after reassembling the sample on the sample holder, the permalloy magnetization is the only varied property. The observed changes of the photoemission distribution originate from the different orientation of the permalloy magnetization and the corresponding orientation of the Néel vector in the antiferromagnetic layer.

Similar experiments were carried out on samples with different thicknesses of permalloy. Using a thinner 1.5-nm-thick permalloy layer results in a better signal-to-background ratio. However, the hysteresis loop is no longer square-shaped and the remanent magnetization is significantly reduced. A thicker (3 nm) permalloy layer exhibits a larger coercive field, but the band structure is barely visible due to the low signal-to-background ratio, which would require unrealistically long data acquisition times.

Photoemission electron microscopy measurements (PEEM) on SiN-capped Mn_2Au films were performed at the SIM beamline of the Swiss Light Source. The sample was illuminated by circularly polarized x-rays at a grazing angle of 16° . The images were normalized to the mean image intensity to consider the different photon intensities for right and left circularly polarized light. The x-ray magnetic circular dichroism (XMCD) image was then calculated as the asymmetry of the images [$A = I^+ - I^- / (I^+ + I^-)$] recorded with right and left circularly polarized light. To plot the XMCD asymmetry, we took the mean value of the asymmetries within the black and white domains [see Fig. 1(a)] over the entire field of view. To obtain the XMCD asymmetry as a function of the incident photon energy, we used the following procedure. In the XMCD image with the most pronounced contrast, we selected a region of interest (ROI), which contained all black (white) domains within the entire field of view, and extracted a mean value of the XMCD asymmetry within the black and white domains separately. The same was done using the same ROI for all the XMCD images acquired at different photon energies. Note that prior to that all the XMCD images were laterally aligned to one another, ensuring that the ROI includes the same domains.

III. RESULTS

A prerequisite for the exceptionally strong exchange bias field required to orient the Néel vector in the antiferromagnetic layer, is the presence of uncompensated magnetic moments of Mn_2Au at its interface with the ferromagnetic layer. The presence of uncompensated moments has been inferred indirectly from the well-defined morphology of the

Mn_2Au surface, which has been shown to display step heights of three atomic layers [26]. Here, we directly probe the Mn surface magnetization using x-ray magnetic circular dichroism (XMCD).

Figure 1(a) shows a photoelectron emission microscopy (PEEM) image of the $\text{Mn}_2\text{Au}(100)$ surface covered by a thin SiN layer, where the XMCD asymmetry reveals the presence of antiferromagnetic domains. The incident x-ray beam, which defines the quantization axis parallel to the magnetic easy axis of the antiferromagnetic film, arrives from the left with a grazing angle of incidence of 16° . The contrast image shows three distinct contrast levels, which are expected if the Néel vector is parallel, antiparallel or perpendicular to the in-plane component of the x-ray photon momentum, analogous to the case of a ferromagnet with fourfold magnetic anisotropy.

The spectral information shown in Fig. 1(b) confirms the previously observed behavior [33] of metallic Mn in Mn_2Au and the pronounced XMCD signal on the rising edge of the Mn L_3 absorption maximum. Specifically, the x-ray absorption spectrum shows the additional presence of a multiplet, indicating partial oxidation of the surface despite the inert capping layer. The appearance of the multiplet structure is very sensitive to oxidation and the observed spectrum indicates an initial oxidation stage (see, e.g., Ref. [34]). Partial oxidation will certainly change the measured XMCD signal and prevent an accurate evaluation of the Mn moments. The XMCD asymmetry [$A = I^+ - I^- / (I^+ + I^-)$] shown in Fig. 1(b) shows a maximum negative value on the rising edge about 1 eV before the maximum absorption intensity in contrast to the usual XMCD, where the difference of the signal for opposite x-ray polarization leads to a maximum XMCD closer to the maximum absorption intensity [35,36].

The XMCD asymmetry could be caused by magnetic moments of Mn atoms at the interface, at step edges, or by atoms interdiffused into the permalloy layer, expecting an opposite magnetic moment with respect to the permalloy magnetization independent on the direction of the Néel vector. The next step is to understand why the XMCD asymmetry is nonzero in view of the collinear antiferromagnetism in Mn_2Au . To explain this observation, we consider the exponentially decreasing electron yield from an atomic layer at a depth z below the surface, as depicted in Figs. 1(c)–1(e). The definition of the Néel vector $\vec{N} = \vec{M}_1 - \vec{M}_2$ includes the sublattice magnetic moments \vec{M}_1 and \vec{M}_2 as shown in Fig. 1(f). Here, \vec{M}_1 denotes the topmost Mn layer, i.e., the Mn layer that is closest to the permalloy capping layer discussed below. Because of the exponentially decreasing contribution with increasing depth, the XMCD asymmetry is dominated by the magnetization of the top Mn layer [Fig. 1(e)]. In combination with the surface morphology of the $\text{Mn}_2\text{Au}(100)$ film, which has step heights of precisely three atomic layers [26], the top Mn layer has the same magnetization orientation on adjacent terraces in the case of an antiferromagnetic domain with homogeneous Néel vector orientation [26].

The escape depth of secondary electrons in metals that are detected in the PEEM measurements is 2.5 nm [37]. Using a simple layer model with a layer distance of $a = 1.423 \text{ \AA}$ to approximate the Mn_2Au structure as sketched in Fig. 1(c), one finds an expected Mn-XMCD asymmetry of 3% of the

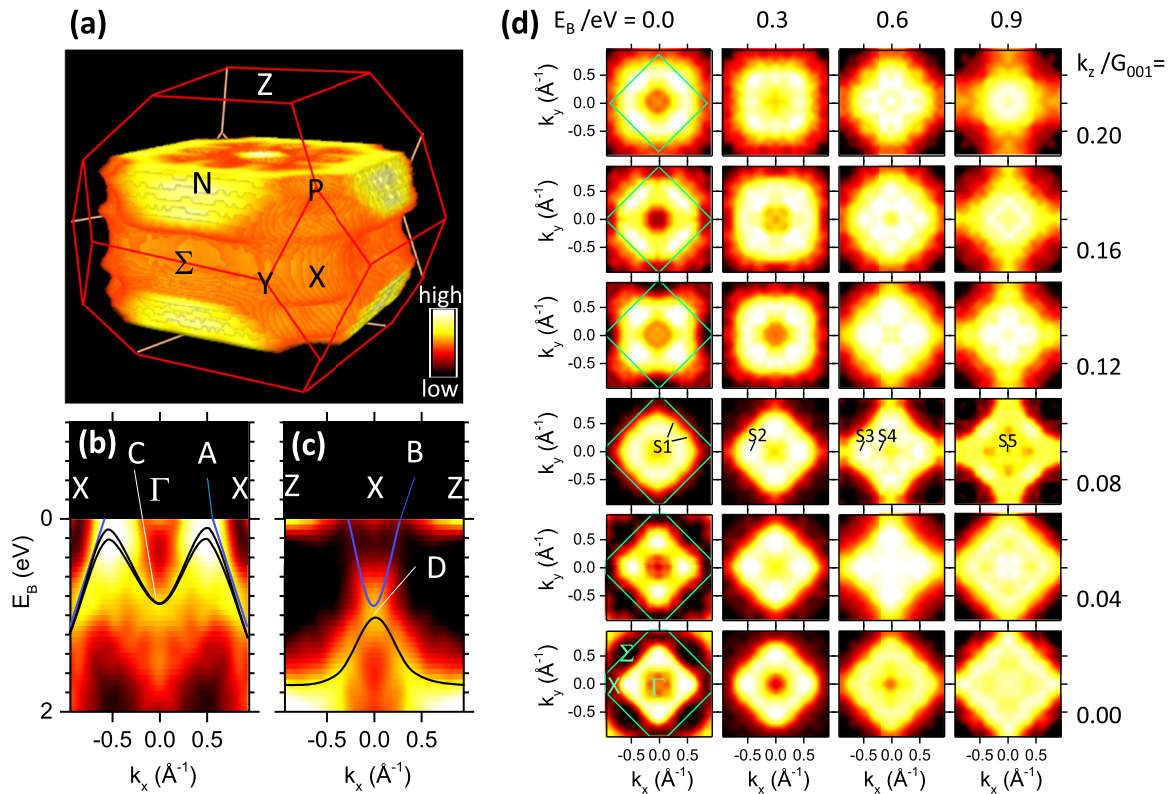


FIG. 2. (a) Three-dimensional representation of the measured spectral density of states of Mn₂Au at the Fermi level $I(E_B = 0, k_x, k_y, k_z)$ (Fermi surface) for $-0.25 < k_z/G_{001} < 0.25$. The indicated Brillouin zone (red lines) of the body centered tetragonal (bct₂) structure of Mn₂Au is based on Ref. [32]. The data were extracted from hard x-ray photoemission excited by a photon energy of 5210 eV at a temperature of 20 K. [(b) and (c)] Band dispersions along the X – Γ – X and Z-X-Z direction, respectively. The color code represents the photoemission intensity from black to white (red-hot) after background subtraction. Full lines denote calculated bands from Ref. [21]. (d) Constant-energy maps of the spectral density of electronic states $I(E_B, k_x, k_y, k_z)$ in planes perpendicular to the c axis. Note that the square areas extend to the Z – Y – Σ plane of the adjacent Brillouin zones towards the corners (Z points) of the images. Perpendicular momentum k_z values are given with respect to the nearest Γ point.

asymmetry from a hypothetical ferromagnetic Mn₂Au film. This is consistent with the experimentally observed maximum XMCD asymmetry of 0.75%, assuming a Mn magnetic moment of about 5 μ_B per atom. Note that the deduced magnetic moment value depends on the assumed escape length of the detected electrons and can only be taken as an estimation.

The surface morphology in combination with the collinear antiferromagnetism in Mn₂Au thus explains the occurrence of the XMCD asymmetry over domains much larger than the typical terrace width of epitaxially grown thin films. The domain sizes observed here are consistent with previously reported magnetic domain sizes with lateral dimensions of 1 μm in epitaxial Mn₂Au films [25]. The top Mn layer thus represents one layer of uncompensated moments, which then result in the strong exchange bias when the Mn₂Au is covered by a permalloy layer.

We now turn to the hard x-ray photoemission experiments. First, we report hard x-ray angular photoemission spectroscopy results on Mn₂Au films where the permalloy film has not been added, providing a reference for the permalloy capped films. In this case, the films exhibit a multi-domain antiferromagnetic state resulting in a symmetric band structure corresponding to the crystal symmetry. We first exploit the fourfold symmetry around the c axis, thus averaging over

the four possible Néel vector directions, to increase the signal-to-noise ratio *via* symmetrization.

Figure 2(a) shows the Fermi surface of Mn₂Au in a three-dimensional color-coded intensity map. Data for different k_z values are derived from repeated Brillouin zones measured simultaneously: The large momentum field of view of 12 \AA^{-1} includes five adjacent Brillouin zones, where increasing parallel momentum results in decreasing perpendicular momentum. This allows us to measure the perpendicular momentum k_z in one experimental run in a range of $\Delta k_z = 0.5G_{001}$ [38]. The k_z interval where photoemission intensity above the background level could be detected is actually smaller ($\Delta k_z = 0.25G_{001}$). This is attributed to a destructive photoelectron interference [39]. Photoemission intensity enhancement or suppression reflects the coherent excitation of photoelectrons from a translational symmetric lattice. At high photon energies, the transition to the final state occurs within high-order repeated Brillouin zones in the normal direction. The photon momentum shifts the final state sphere by more than one Brillouin zone radius in the parallel momentum direction and to a fraction of the Brillouin zone in the (negative) normal direction. This shift opens constructive and destructive interference conditions. With the reciprocal lattice vector G_z perpendicular to the surface and the final state electron

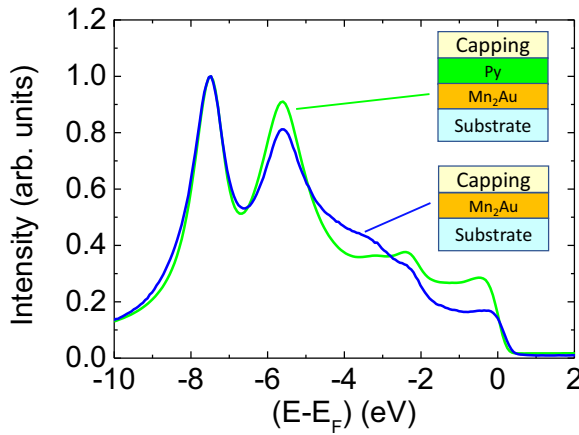


FIG. 3. Energy distribution curves obtained from integrating the photoemission intensity over the parallel momentum for a photon energy of 5210 eV for the sample without permalloy layer and 5185 eV for the sample with permalloy capping. The binding energy is $E_B = -(E - E_F)$. The intensities are normalized at the peak near $E_B = 8$ eV.

momentum k_f , we obtain the corresponding relation in momentum space $k_f = (2n - 1)/2G_z$ for destructive interference [39]. For given photon energy, lattice constants, and angle of incidence, we obtain constructive interference for $\Delta k_z = 0.0 G_{001}$ and destructive interference for $\Delta k_z = 0.5 G_{001}$.

The experimentally obtained Fermi surface is in qualitative agreement with the theoretically predicted Fermi surface reported in Ref. [21]. In particular, the diamond-shaped cross section in the $\Gamma - X - \Sigma$ plane agrees well with calculations. Furthermore, the high intensity observed near the N points corresponds to the calculated tubular bands crossing the $N - Y - P$ plane.

The band dispersions shown in Figs. 2(b) and 2(c) are derived from slices through the four-dimensional array $I(E_B, k_x, k_y, k_z)$, where the k_z value has been determined with a better accuracy as compared to the experimental results reported in Ref. [21]. For the band dispersion representation, the intensity has been normalized to the momentum-integrated intensity (Fig. 3). The normalization removes the variation of the photoemission intensity due to the localized Au $5d$ states and due to quasielastic phonon scattering [38].

The inverted parabolic band A, shown in Fig. 2(b) along the $\Gamma - X$ profile, has an apex above the Fermi level. The band crosses the Fermi level near 0.5 \AA^{-1} and forms the Fermi surface. The band C, which is below band A, disperses to a larger binding energy as it approaches the Γ point, forming maxima near $k_x = \pm 0.5 \text{ \AA}^{-1}$ and a minimum at Γ . This central minimum of band C appears at $E_B = 0.9$ eV, in very good agreement with previously reported results [21], and deviates from the calculated binding energy of $E_B = 0.5$ eV, revealing a shift of 400 meV to higher binding energies, due to electron correlation effects not included in the theoretical model. The energy broadening of band C near $k_x = \pm 0.5 \text{ \AA}^{-1}$ is associated with the splitting of band C at $|k_x| > \pm 0.4 \text{ \AA}^{-1}$ [21], which is a result of the spin-orbit coupling and thus depends on the orientation of the Néel vector. Note that the averaging over magnetic domains prevents the observation of the band asymmetries in this configuration.

The E_B versus k_x section along the Z-X-Z direction [Fig. 2(c)] shows a prominent band D near the Z point at $E_B = 1.7$ eV and at X at $E_B = 1$ eV. In this case, the binding energy is in agreement with the calculated results [21]. The broadening of the band D observed for $|k_x| > \pm 0.4 \text{ \AA}^{-1}$ is again related to the spin-orbit coupling. The parabolic band B shows an apex at the X point at $E_B = 1$ eV. For band B we find a good agreement with the calculated values given in Ref. [21]. The band gap between bands B and D at this position depends on the Néel vector orientation and vanishes in the domain averaged data used here. The photoemission intensity at the Z points near the Fermi level is probably associated with bands forming the Fermi surface in the Z - Σ - Y plane, which appear with weak intensity due to a small photoemission matrix-element [16].

Figure 2(d) shows sections through the four-dimensional data set $I(E_B, k_x, k_y, k_z)$ at the given perpendicular moments k_z and binding energies E_B . This plot serves as a reference for the photoemission results obtained on Néel vector aligned Mn_2Au films capped with the ferromagnetic permalloy layer.

The energy distribution curves integrated over the parallel momentum at $k_z = 0$, shown in Fig. 3, compare films with and without permalloy layer capping. The prominent peaks near the binding energies $E_B = 6$ and 8 eV are due to the localized Au $5d$ states in the Mn_2Au film [40]. Note that the high photon energy causes an increase of the photoemission probability with increasing orbital momentum. The energy distribution shows that the Au $5d$ peaks are almost unchanged after the capping with permalloy, confirming the increased inelastic mean free path at this high photon energy. The photoemission intensity for the capped sample is increased in the range $E_B < 2$ eV. This corresponds to the broad photoemission intensity maximum that is observed for bulk permalloy in this energy range [41]. It is therefore expected that the photoemission intensity near the Fermi level originating from Mn_2Au is enhanced by an unstructured background intensity photoexcited from the permalloy layer. The top SiN layer, which prevents oxidation of the film stack, has an energy gap in this binding energy range and therefore does not lead to additional photoelectrons.

Figures 4(a)–4(d) show the momentum-resolved photoemission intensity for the sample with the permalloy layer. The increase of the elastic background intensity without momentum information is twofold compared to the uncapped Mn_2Au film because of the additional photoemission yield from the permalloy layer. In addition, the probability that photoelectrons excited in the Mn_2Au layer are scattered by phonons in the permalloy layer during the motion towards the surface adds up to the Debye-Waller scattering occurring in the Mn_2Au layer itself. Due to the limited energy resolution in the hard x-ray regime, these quasi-elastic electrons also add up to the momentum-independent background intensity. Hence, the background intensity relative to the direct photoemission intensity is significantly larger than in the case of films without a permalloy layer.

To increase the signal-to-background ratio, we symmetrized the constant energy maps according to the fourfold crystal symmetry around the c -axis. In principle, the homogeneous background intensity can be subtracted from the measured data. However, the signal-to-noise ratio is determined

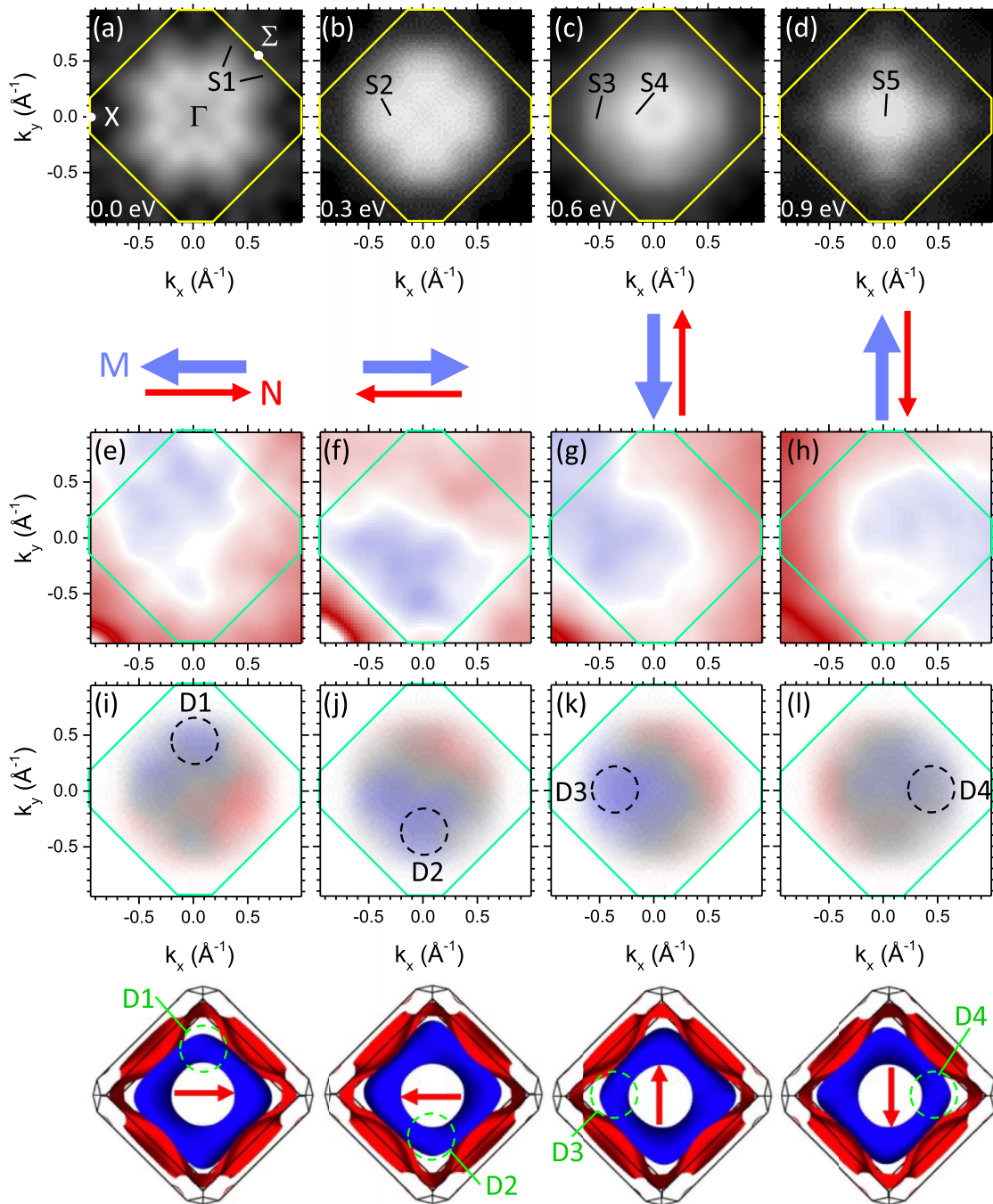


FIG. 4. [(a)–(d)] Symmetrized constant energy maps of the intensity distribution for $\text{Mn}_2\text{Au}(100)$ capped with 2 nm permalloy (Py) and 2 nm SiN protective layer measured at a photon energy of 5185 eV. The binding energy increases from (a) 0 (E_F), (b) 0.3, (c) 0.6, to (d) 0.9 eV. Yellow lines indicate the Brillouin zone cut in the $\Gamma - X - \Sigma$ plane. [(e)–(h)] Intensity difference maps $D(k_x, k_y) = I(E_B = 0.5 \text{ eV}, k_x, k_y) - I(E_B = 0.2 \text{ eV}, k_x, k_y)$ for the indicated magnetization orientation (M) in the Py layer and the corresponding Néel vector orientation (N). Red/blue color indicates positive/negative difference values. [(i)–(l)] Difference and intensity depicted in a combined color scale. The difference in experimental intensities stems from integration over energy and momentum ranges given by the experimental resolution. Bottom row: Calculated constant energy surfaces in momentum space at $E_B = 0.4 \text{ eV}$ for the indicated Néel vectors N (red arrows). The red surface relates to band A [Fig. 2(b)] and the blue asymmetric surface to band C. (Calculated data from Ref. [16].)

by the total measured intensity. Therefore, increasing the background intensity about fourfold, as in the case of the 2 nm permalloy capping, would require an increase in acquisition time by a factor of 16 to achieve the same data quality or to sacrifice momentum resolution by binning. This explains the decreased effective momentum resolution in Figs. 4(a)–4(d).

The symmetrized results shown in Figs. 4(a)–4(d) confirm that the capping with permalloy still allows the band structure of the epitaxial Mn_2Au film beneath the permalloy layer to be observed. The sequence of constant energy maps for binding energies between 0 and 0.9 eV for a photon energy of 5185 eV agrees with the reference data for similar films without the

permalloy capping for $k_z/G_{001} = 0.08$ (see Fig. 2). The deviation from $k_z/G_{001} = 0.0$ is due to the slightly lower photon energy set for this experiment.

The value of k_z/G_{001} , defined by the photon energy, was deliberately chosen because the asymmetry due to the Néel vector orientation is larger for the planar section above the Γ point, as discussed below. To compare the constant energy sections of the intensity array at the selected binding energies with the results shown in Fig. 2, the relevant band features are highlighted below. The Fermi surface is characterized by the split structure (S1) near the Σ point [Fig. 4(a)]. This feature is caused by band A crossing the Fermi level and is also seen in Fig. 2(d). At the larger binding energy $E_B = 0.3$ eV, the highest intensity in the constant energy map shown in Fig. 4(b) is along the $\Gamma - X$ direction (S2). This intensity maximum also appears in Fig. 2(d). This increased intensity is due to the band C, which has a maximum at $E_B = 0.2$ eV and crosses the constant energy section of $E_B = 0.3$ eV between the Γ and X points. It is this band that splits up due to the spin-orbit coupling and causes the band asymmetry. At $E_B = 0.6$ eV, band C crosses the constant energy map at two parallel momentum values, one closer to the X point and one closer to the Γ point [see Fig. 2(c)]. These crossings cause the intensity extensions S3 and S4 in the constant energy maps shown in Figs. 4(c) and 2(d), forming a diamond-like intensity distribution. The spin-orbit splitting at this binding energy has dropped to almost zero. At $E_B = 0.9$ eV, the diamond-like intensity distribution in the constant energy map is even more pronounced due to the energy dispersion of band C. The band minimum of band C causes a high intensity near the Γ point (S5) as observed in Figs. 4(d) and 2(d). The above similarities provide good agreement between the photoemission data measured for the permalloy capped Mn_2Au film and the uncapped reference sample. Therefore, the data confirms that the Mn_2Au band structure can be detected beneath the permalloy film. Details of the Fermi surface, such as the separation of the blue and red bands in Fig. 4 are not resolved due to the limited energy resolution.

Finally, we discuss the nonsymmetrized data for the samples with different permalloy magnetization directions. We subtract the photoemission intensity recorded at two different binding energies for each sample piece, $D(k_x, k_y) = I(E_B = 0.5 \text{ eV}, k_x, k_y) - I(E_B = 0.2 \text{ eV}, k_x, k_y)$. The result is shown in Figs. 4(e)–4(h). The choice of these two binding energies is based on the fact that the intensity distribution at $E_B = 0.2$ eV is almost symmetric, and the distribution at $E_B = 0.5$ eV shows a maximum asymmetry caused by the Néel vector direction. Additional intensity gradients are significantly reduced for the differential intensity distribution.

The difference map shown in Fig. 4(e) shows a negative (blue) value near the top of the map and a positive (red) value near the bottom of the map. The large positive asymmetry in the lower left corner is due to an image artifact near the detector boundary and is present in all four maps in Figs. 4(e)–4(h). Figure 4(f) shows the result for the permalloy layer magnetized in the opposite direction. In this case, the negative value occurs near the bottom of the figure, while the difference is positive near the top of this figure. A similar systematic change in sign can be observed for the cases of the permalloy magnetization pointing down [Fig. 4(g)] and up [Fig. 4(h)],

where the difference value is negative on the left side and positive on the right side [Fig. 4(g)] or vice versa [Fig. 4(h)]. To further remove artifacts of the intensity recording, we plot the data in a combined difference and intensity representation [Figs. 4(i)–4(l)], where the difference data are shown only in the relevant momentum regions with high photoemission intensity. In Fig. 4(i), the reduced photoemission intensity (blue) can be seen all the way to the top of the image. In Figs. 4(j)–4(k), the blue color (negative difference) appears at the bottom, left, and right, respectively.

We compare the experimental results with the calculated constant energy contours in the three-dimensional momentum space of Ref. [16] (see bottom row of Fig. 4). Two band features contribute to the constant energy surface at a binding energy of 0.4 eV, indicated in red and blue colors. The red constant energy surface belongs to band A and the blue surface belongs to band B [see Fig. 2(b) for band definition]. The spin-orbit splitting combined with the broken local inversion symmetry leads to the asymmetry of the band structure. This asymmetry manifests itself as a pronounced depression of the blue surface to the top in the left panel (D1). This depression shows in the opposite direction for the opposite Néel vector direction (D2). The systematic change of the orientation of the depression with the orientation of the Néel vector direction is also observed for the other two directions (D3 and D4). The depression always points to the left when looking in the direction of the Néel vector. The depression of the constant energy surface causes a smaller photoemission intensity in particular in a perpendicular momentum (k_z) plane slightly above the Γ point, where the plane does not intersect the band B surface in the region of the depression. As a consequence, one observes a reduced photoemission intensity in the regions D1–D4.

To conclude, the result indicates an asymmetric photoemission intensity distribution in reciprocal space. The larger intensity occurs for an in-plane moment direction $\vec{n} \times \vec{M}$, where \vec{M} denotes the remanent permalloy magnetization and \vec{n} the surface normal. From theory (see the bottom panel of Fig. 4), we learn that a higher intensity occurs for an in-plane moment direction $-\vec{n} \times \vec{N}$ (extended blue area), where \vec{N} is the Néel vector. Thus our experimental result shows that \vec{N} is antiparallel to \vec{M} . This implies that the top Mn layer in the Mn_2Au film has a magnetic moment antiparallel to the magnetic moments of the Permalloy.

IV. SUMMARY

We experimentally observe a broken symmetry of the band structure in $\text{Mn}_2\text{Au}(001)$ epitaxial thin films capped with a 2 nm permalloy film, which is caused by the homogeneous orientation of the Néel vector. The homogeneous orientation of the Néel vector is made possible by the exceptionally strong exchange bias field, which allows the Néel vector to be controlled by the direction of the permalloy magnetization. XMCD-PEEM images show that a full layer of completely uncompensated Mn moments is responsible for this exchange bias.

The broken symmetry of the band structure is most pronounced at a binding energy of 0.3–0.4 eV. We observed a maximum asymmetry of 1% probed by bulk-sensitive hard

x-ray photoemission spectroscopy. The Néel vector induced parity violation of the crystallographic symmetry, visible in the photoelectron momentum patterns, is consistent with previously published band structure calculations.

The band asymmetry, $E(k) \neq E(-k)$, allows the Néel vector orientation to be assigned with respect to the permalloy magnetization. We find an antiparallel orientation of the Néel vector direction and the permalloy magnetization, indicating an antiparallel orientation of the top Mn layer and the permalloy magnetic moments.

ACKNOWLEDGMENTS

Funding by the Deutsche Forschungsgemeinschaft (DFG, German Research Foundation) – TRR Grant No. 173-268565370 (Projects A01, A02, and A05) and Scho 341/16-1 as well as BMBF Grant No. 05K19UM4 is gratefully acknowledged. We acknowledge the Paul Scherrer Institut, Villigen, Switzerland, for the beamtime at the SIM beamline of the Swiss Light Source and we thank the SIM beamline staff for technical support.

- [1] T. Jungwirth, X. Marti, P. Wadley, and J. Wunderlich, *Nat. Nanotechnol.* **11**, 231 (2016).
- [2] O. Gomonay, T. Jungwirth, and J. Sinova, *Phys. Stat. Sol. RRL* **11**, 1700022 (2017).
- [3] V. Baltz, A. Manchon, M. Tsoi, T. Moriyama, T. Ono, and Y. Tserkovnyak, *Rev. Mod. Phys.* **90**, 015005 (2018).
- [4] S. Reimers, Y. Lytvynenko, Y. R. Niu, E. Golias, B. Sarpi, L. S. I. Veiga, T. Denneulin, A. Kovács, R. E. Dunin-Borkowski, J. Bläßer, M. Kläui, and M. Jourdan, *Nat. Commun.* **14**, 1861 (2023).
- [5] V. Grigorev, M. Filianina, S. Y. Bodnar, S. Sobolev, N. Bhattacharjee, S. Bommanaboyena, Y. Lytvynenko, Y. Skourski, D. Fuchs, M. Kläui, M. Jourdan, and J. Demsar, *Phys. Rev. Appl.* **16**, 014037 (2021).
- [6] J. Železný, H. Gao, K. Vyborny, J. Zemen, J. Masek, A. Manchon, J. Wunderlich, J. Sinova, and T. Jungwirth, *Phys. Rev. Lett.* **113**, 157201 (2014).
- [7] P. Wadley, B. Howells, J. Zelezny, C. Andrews, V. Hills, R. P. Champion, V. Novak, K. Olejnik, F. Maccherozzi, S. S. Dhesi, S. Y. Martin, T. Wagner, J. Wunderlich, F. Freimuth, Y. Mokrousov, J. Kunes, J. S. Chauhan, M. J. Grzybowski, A. W. Rushforth, K. W. Edmonds *et al.*, *Science* **351**, 587 (2016).
- [8] M. J. Grzybowski, P. Wadley, K. W. Edmonds, R. Beardsley, V. Hills, R. P. Champion, B. L. Gallagher, J. S. Chauhan, V. Novak, T. Jungwirth, F. Maccherozzi, and S. S. Dhesi, *Phys. Rev. Lett.* **118**, 057701 (2017).
- [9] P. Wadley, S. Reimers, M. J. Grzybowski, C. Andrews, M. Wang, J. S. Chauhan, B. L. Gallagher, R. P. Champion, K. W. Edmonds, S. S. Dhesi, F. Maccherozzi, V. Novak, J. Wunderlich, and T. Jungwirth, *Nat. Nanotech.* **13**, 362 (2018).
- [10] S. Y. Bodnar, L. Šmejkal, I. Turek, T. Jungwirth, O. Gomonay, J. Sinova, A. A. Sapozhnik, H. J. Elmers, M. Kläui, and M. Jourdan, *Nat. Commun.* **9**, 348 (2018).
- [11] M. Meinert, D. Graulich, and T. Matalla-Wagner, *Phys. Rev. Appl.* **9**, 064040 (2018).
- [12] J. Godinho, H. Reichlova, D. Kriegner, V. Novak, K. Olejnik, Z. Kaspar, Z. Soban, P. Wadley, R. P. Champion, R. M. Otxoa, P. E. Roy, J. Zelezny, T. Jungwirth, and J. Wunderlich, *Nat. Commun.* **9**, 4686 (2018).
- [13] M. Arana, M. Gamino, E. F. Silva, V. M. T. S. Barthem, D. Givord, A. Azevedo, and S. M. Rezende, *Phys. Rev. B* **98**, 144431 (2018).
- [14] X. Chen, X. Zhou, R. Cheng, C. Song, J. Zhang, Y. Wu, Y. Ba, H. Li, Y. Sun, Y. You, Y. Zhao, and F. Pan, *Nat. Mater.* **18**, 931 (2019).
- [15] A. G. Linn, P. Hao, K. N. Gordon, D. Narayan, B. S. Berggren, N. Speiser, S. Reimers, R. P. Champion, V. Novák, S. S. Dhesi, T. K. Kim, C. Cacho, L. Šmejkal, T. Jungwirth, J. D. Denlinger, P. Wadley, and D. S. Dessau, *npj Quantum Mater.* **8**, 19 (2023).
- [16] O. Fedchenko, L. Šmejkal, M. Kallmayer, Y. Lytvynenko, K. Medjanik, S. Babenkov, D. Vasilyev, M. Kläui, J. Demsar, G. Schönhense, M. Jourdan, J. Sinova, and H. J. Elmers, *J. Phys.: Condens. Matter* **34**, 425501 (2022).
- [17] L. Šmejkal, J. Zelezny, J. Sinova, and T. Jungwirth, *Phys. Rev. Lett.* **118**, 106402 (2017).
- [18] L. Šmejkal, Y. Mokrousov, B. Yan, and A. H. MacDonald, *Nat. Phys.* **14**, 242 (2018).
- [19] S. Hayami, M. Yatsushiro, Y. Yanagi, and H. Kusunose, *Phys. Rev. B* **98**, 165110 (2018).
- [20] H. Watanabe and Y. Yanase, *Phys. Rev. X* **11**, 011001 (2021).
- [21] H. J. Elmers, S. V. Chernov, S. W. D'Souza, S. P. Bommanaboyena, S. Y. Bodnar, K. Medjanik, S. Babenkov, O. Fedchenko, D. Vasilyev, S. Y. Agustsson, C. Schlueter, A. Gloskovskii, Y. Matveyev, V. N. Strocov, Y. Skourski, L. Šmejkal, J. Sinova, J. Minar, M. Kläui, G. Schönhense *et al.*, *ACS Nano* **14**, 17554 (2020).
- [22] S. Hayami, Y. Yanagi, and H. Kusunose, *Phys. Rev. B* **102**, 144441 (2020).
- [23] S. Schulz, A. Y. Vyazovskaya, G. Poelchen, A. Generalov, M. Güttler, M. Mende, S. Danzenbächer, M. M. Otrokov, T. Balasubramanian, C. Polley, E. V. Chulkov, C. Laubschat, M. Peters, K. Kliemt, C. Krellner, D. Y. Usachov, and D. V. Vyalikh, *Phys. Rev. B* **103**, 035123 (2021).
- [24] C. Carbone, P. Moras, P. M. Sheverdyeva, D. Pacilé, M. Papagno, L. Ferrari, D. Topwal, E. Vescovo, G. Bihlmayer, F. Freimuth, Y. Mokrousov, and S. Blügel, *Phys. Rev. B* **93**, 125409 (2016).
- [25] A. A. Sapozhnik, M. Filianina, S. Y. Bodnar, A. Lamirand, M.-A. Mawass, Y. Skourski, H.-J. Elmers, H. Zabel, M. Kläui, and M. Jourdan, *Phys. Rev. B* **97**, 134429 (2018).
- [26] S. Bommanaboyena, B. Backes, L. S. I. Veiga, S. S. Dhesi, Y. R. Niu, B. Sarpi, T. Denneulin, A. Kovacs, T. Mashoff, O. Gomonay, J. Sinova, K. Everschor-Sitte, D. Schönke, R. M. Reeve, M. Kläui, H.-J. Elmers, and M. Jourdan, *Nat. Commun.* **12**, 6539 (2021).
- [27] M. Jourdan, H. Braeuning, A. Sapozhnik, H. J. Elmers, H. Zabel, and M. Kläui, *J. Phys. D: Appl. Phys.* **48**, 385001 (2015).
- [28] S. P. Bohammaboyena, T. Bergfeldt, R. Heller, M. Kläui, and M. Jourdan, *J. Appl. Phys.* **127**, 243901 (2020).
- [29] K. Medjanik, O. Fedchenko, S. Chernov, D. Kutnyakhov, M. Ellguth, A. Oelsner, B. Schönhense, T. R. F. Peixoto, P. Lutz, C. H. Min, F. Reinert, S. Däster, Y. Acremann, J. Viehhaus, W. Wurth, H. J. Elmers, and G. Schönhense, *Nat. Mater.* **16**, 615 (2017).

- [30] K. Medjanik, S. V. Babenkov, S. Chernov, D. Vasilyev, B. Schönhense, C. Schlueter, A. Gloskovskii, Y. Matveyev, W. Drube, H. J. Elmers, and G. Schönhense, *J. Synchrotron Rad.* **26**, 1996 (2019).
- [31] M. P. Seah and W. A. Dench, *Surf. Interface Anal.* **1**, 2 (1979).
- [32] W. Setyawan and S. Curtarolo, *Comput. Mater. Sci.* **49**, 299 (2010).
- [33] A. A. Sapozhnik, R. Abrudan, Y. Skourski, M. Jourdan, H. Zabel, M. Kläui, and H. J. Elmers, *Phys. Stat. Sol. Rapid Res. Lett.* **11**, 1600438 (2017).
- [34] M. Kallmayer, H. J. Elmers, B. Balke, S. Wurmehl, F. Emmerling, G. H. Fecher, and C. Felser, *J. Phys. D* **39**, 786 (2006).
- [35] P. Klaer, M. Kallmayer, H. J. Elmers, L. Basit, J. Thöne, S. Chadov, and C. Felser, *J. Phys. D* **42**, 084001 (2009).
- [36] A. A. Sapozhnik, C. Luo, H. Ryll, F. Radu, M. Jourdan, H. Zabel, and H.-J. Elmers, *Phys. Rev. B* **97**, 184416 (2018).
- [37] R. Nakajima, J. Stöhr, and Y. U. Idzerda, *Phys. Rev. B* **59**, 6421 (1999).
- [38] S. Y. Agustsson, S. V. Chernov, K. Medjanik, S. Babenkov, O. Fedchenko, D. Vasilyev, C. Schlueter, A. Gloskovskii, Y. Matveyev, K. Kliemt, C. Krellner, J. Demsar, G. Schönhense, and H.-J. Elmers, *J. Phys.: Condens. Matter* **33**, 205601 (2021).
- [39] G. Schönhense, K. Medjanik, S. Babenkov, D. Vasilyev, M. Ellguth, O. Fedchenko, S. Chernov, B. Schönhense, and H. J. Elmers, *Commun. Phys.* **3**, 45 (2020).
- [40] J. Rubio-Zuazo and G. R. Castro, *Rev. Adv. Mat. Sci.* **15**, 79 (2007), Symposium on Complex Oxide Materials for New Technologies held at the 2006 E-MRS Fall Meeting, Warsaw, Poland, September 04–08, 2006.
- [41] K. N. Altmann, D. Y. Petrovykh, and F. J. Himpsel, *Surf. Sci. Spectra* **6**, 255 (1999).